

Trusted Inertial Terrain-Aided Navigation (TITAN)

Tucker Haydon, *Sandia National Laboratories*

Todd E. Humphreys, *The University of Texas at Austin*

Preprint of paper published in the proceedings of ION GNSS+ 2023

Trusted Inertial Terrain-Aided Navigation (TITAN)

Tucker Haydon, *Sandia National Laboratories*

Todd E. Humphreys, *The University of Texas at Austin*

BIOGRAPHY

Tucker Haydon Tucker Haydon is a Navigation Engineer at Sandia National Labs, and a PhD student in Aerospace Engineering at the University of Texas at Austin. His research is focused on radar-based terrain-aided navigation.

Todd E. Humphreys Todd E. Humphreys (B.S., M.S., Utah State University; Ph.D., Cornell University) holds the Ashley H. Priddy Centennial Professorship in Engineering in the department of Aerospace Engineering and Engineering Mechanics at the University of Texas at Austin. He is Director of the Wireless Networking and Communications Group and of the UT Radionavigation Laboratory, where he specializes in the application of optimal detection and estimation techniques to positioning, navigation, and timing. His awards include the UT Regents' Outstanding Teaching Award (2012), the NSF CAREER Award (2015), the ION Thurlow Award (2015), and the PECASE (NSF, 2019). He is Fellow of the Institute of Navigation and of the Royal Institute of Navigation.

Abstract

The vertical synthetic aperture radar (VSAR) is proposed as a navigation sensor, and a companion navigation algorithm – Trusted Inertial Terrain-Aided Navigation (TITAN) – is introduced. The TITAN algorithm consumes vector range-Doppler measurements produced by a VSAR and correlates them against a local digital terrain elevation map with an extended Kalman filter, enabling accurate navigation without the need for GPS. The navigation accuracy of the VSAR/TITAN combination is quantified with post-processed flight data, and shown to be within 15 meters.

I. INTRODUCTION

The digital age has ushered in a new era of remote navigation systems. What was once a dream — autonomous cars, air taxis, automated airliner takeoff & landing systems, unmanned spacecraft landing systems, and reusable rocket booster systems, to name a few — are quickly nearing realization. With these technologies comes a need for accurate, robust, and trusted navigation systems that must operate in environments where Global Navigation Satellite System (GNSS) signals may be obstructed, degraded, unavailable, or simply insufficient alone to meet system requirements. Remote spacecraft navigation and landing is one such problem. GNSS is unavailable to remote spacecraft landers, and so they must rely on a combination of alternative navigation technologies to safely guide their descent. For example, the recent Mars rover landers leveraged a combination of optical aerial image registration and radar altimeters to guide their descent [Johnson et al., 2022]. While sufficient for these missions, optical image registration may be infeasible for low-light missions such as near the Moon's poles or landings on celestial bodies covered by weather and clouds (e.g., Venus or Titan). In such cases, terrain-aided navigation (TAN) techniques leveraging radars, LIDARs, or laser range finders could be suitable navigation alternatives as all these sensors can operate in the dark and some in the presence of cloud cover.

Terrain-aided navigation is one of the oldest techniques of global, unambiguous navigation. Terrain-aided navigation correlates ranging measurements to the ground against a local terrain elevation map to determine the position of the sensor. The technology dates back to the 1950s where it was primarily developed for cruise missile applications [Golden, 1980]. Today, radar altimeters and terrain-aided navigation can be found in a variety of applications including remote spacecraft landers, such as the Martian and lunar landers, and aircraft terrain awareness and warning systems [Johnson et al., 2022, fed, 1974].

Since its inception in the 1950s, terrain-aided navigation has developed into two broad families of techniques: single-beam and multi-beam. Single-beam techniques typically employ a laser range finder, narrow-beam radar, or interferometric radar to measure the range to a single ground point. For example, Sandia National Labs suggested measuring the ground clearance (range to the nadir point) with a radar altimeter [Hostetler and Andreas, 1983]; and, recently, Carroll and Canciani proposed using a steerable laser sensor to measure the slant range to a nearby point of ‘high information’ [Carroll and Canciani, 2021]. Multi-beam techniques typically employ a LIDAR or an array of radars to measure the range to many overflown ground points. For example, Johnson and Ivanov proposed using a LIDAR sensor to create a three-dimensional point cloud measurement of overflown terrain [Johnson and Ivanov, 2011]; and Reed and Gaudet et al. each suggested using three individual radar beams to measure the slant ranges along three different vectors [Reed et al., 1980, Gaudet and Furfar, 2013].

Single-beam techniques often result in a less-accurate navigation system: it is difficult to precisely and unambiguously estimate the three-dimensional position, velocity, and attitude of a system — a total of nine states — from a single measurement. As a result, single-beam techniques often resort to particle filters to handle observability and convergence concerns [Hollowell, 1990, Zhao et al., 2014, Lee et al., 2020]. Multi-beam techniques are often more accurate than single-beam techniques due to diversified measurement geometries and a general increase in the available measurement information. This gain in navigation accuracy, however, has historically come at a cost. Multi-antenna systems require greater complexity, size, weight, and power (SWaP) than single-antenna systems — a cost not easily accepted by remote navigation systems with limited SWaP constraints. LIDAR sensors do not require multiple antennas, though they are often limited in sensing range, and their performance is degraded by weather.

Synthetic aperture radars (SARs) span the single- and multi-beam families, and take the best properties from the two: SARs are *single-antenna* radar systems that produce *vector* products. Specifically, SARs emit a series of linear, frequency-modulated pulses (chirps) from a single antenna and coherently recombine the ground-reflected returns into a two-dimensional image. This *coherent* recombination of *many* pulses facilitates the two-dimensional image formation from a single antenna. There are two more properties of SARs which further enhance their allure as a navigation sensor: (1) SARs are generally unaffected by weather; and (2) SAR images can be formed at much greater standoff distances than LIDARs. The former property is guaranteed provided that the radar center frequency is far from weather attenuation bands, and the latter is guaranteed by the SAR's ability to coherently recombine reflected signals over longer intervals than LIDARs, yielding measurements with higher signal-to-noise ratios.

SARs can generally be classified into two types of sensors based on their sensing geometry: side-looking SARs and vertical SARs (VSARs). Side-looking SAR systems point the radar in the cross-track direction of flight, and the resulting image product is an optical-like image that primarily senses terrain *reflectivity*. VSAR systems point the radar in the downward direction of flight, and the resulting product is a range-Doppler image that primarily senses terrain *elevation*. This difference in SAR image product fundamentally changes the downstream navigation processing: side-looking SAR images must be correlated against terrain *reflectivity* maps, while VSAR images must be correlated against terrain *elevation* maps. For this reason, side-looking and vertical SARs should be considered two different navigation sensors as their sensed and reference data products represent two different properties of terrain.

While several recent publications have suggested using side-looking SARs for navigation [Lindstrom et al., 2022, Pogorelsky et al., 2022], the use of vertical synthetic aperture radar for navigation has been almost completely overlooked. Perhaps the closest suggestion is Choi et al. [Choi et al., 2013] who suggested using Doppler beam sharpening to resolve the zero-Doppler bin of a Frequency Modulated Continuous Waveform (FMCW) radar altimeter, but they stopped short of full synthetic aperture processing and vector measurements. Several groups have proposed using an interferometric radar altimeter that relies on synthetic aperture processing [Kim et al., 2018, Oh et al., 2019], but interferometry requires multiple antennas. Ultimately, proposed radar altimetry navigation techniques seemed to have jumped from simple ground clearance systems to complex interferometric systems, overstepping the intermediate possibilities of synthetic aperture radars.

Despite the benefits of VSARs — single antenna, vector measurements, all-weather, and large standoff distances —, they are underexplored as a navigation technology. This paper addresses this exploration gap. Its are the following: (1) the proposal to use a vertical synthetic aperture radar as a navigation sensor; (2) the introduction of a companion navigation algorithm leveraging the VSAR image products — the Trusted Inertial Terrain-Aided Navigation (TITAN) algorithm; and (3) a demonstration of the VSAR / TITAN combination with captured radar data.

II. VERTICAL SYNTHETIC APERTURE RADAR

The following section introduces background information on the VSAR and derives its signal model.

1. Background

The vertical synthetic aperture radar is a twist on the classic side-looking synthetic aperture radar. Instead of pointing the radar in the cross-track direction of an airborne platform, the SAR is pointed directly down towards the ground. The VSAR still operates like a side-looking SAR, transmitting a series of pulses and coherently recombining the ground-reflected returns, but the imaging geometry changes the fundamental image product. Instead of producing an optical-like image, the VSAR produces a range-Doppler image of illuminated terrain.

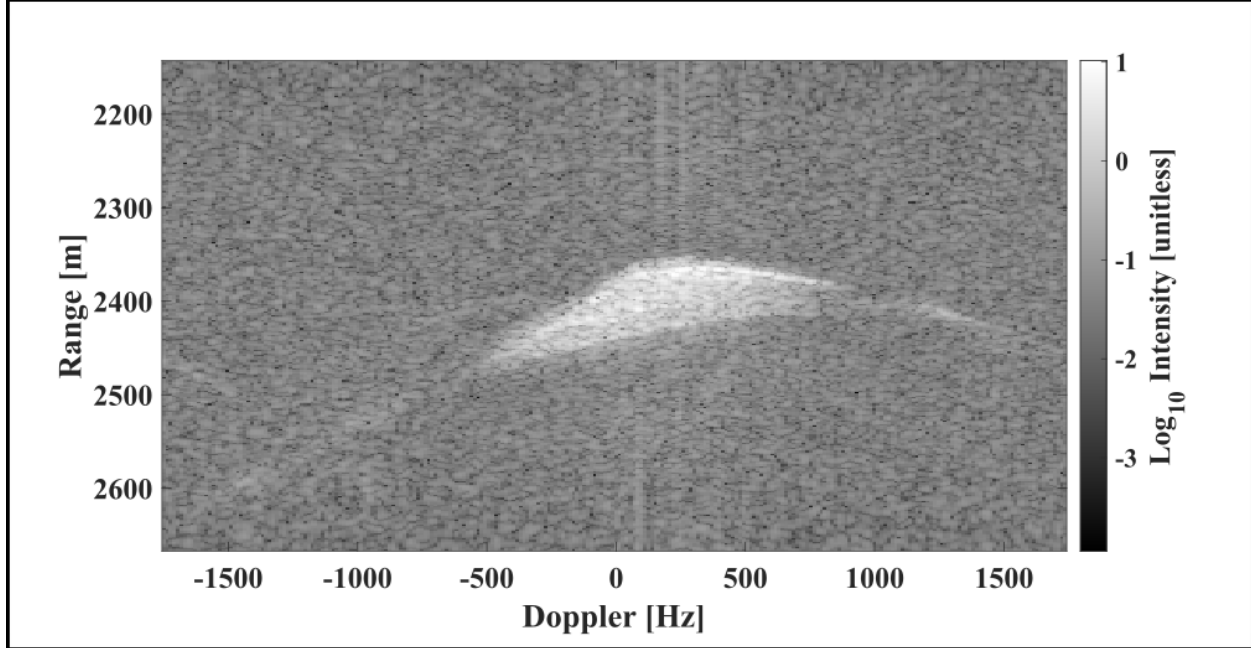


Figure 1: Vertical synthetic aperture radar range-Doppler image

Fig. 1 depicts a range-Doppler image produced by Sandia National Labs' (SNL's) testbed VSAR system overflying a wilderness area in central New Mexico. Range is marked along the vertical axis and *increases down*, while Doppler is marked on the horizontal axis and increases from left-to-right. The pixel color represents the intensity of the reflected radar signal: a bright white pixel indicates a strong return at the associated range-Doppler coordinate while a dark pixel indicates a weak return or lack of return. Generally, in Fig. 1, the white region in the center of the image corresponds with illuminated terrain, the dark region above the white region corresponds with air between the radar and the terrain, and the dark region to the sides and below the white region corresponds with air or terrain whose reflected signal is attenuated below the image's noise floor.

Despite using the same sensor and signal processing techniques as a side-looking SAR, the VSAR range-Doppler image in Fig. 1 looks nothing like an optical image. In fact, the closest analog to the VSAR range-Doppler image is a LIDAR point cloud: a LIDAR measures the three-dimensional Cartesian offsets to illuminated terrain, and a VSAR measures the two-dimensional range-Doppler offset to illuminated terrain.

There exist many different SAR image processing algorithms that perform the coherent recombination — Range Doppler, Chirp Scaling, Omega K, Spectral Analysis (SPECAN), Backprojection, Polar Format, and Overlapped Subaperture to name a few [[Cumming and Wong, 2005](#), [Doerry, 1995](#)]. Each of these methods exists to solve a particular problem with radar signal processing such as computational complexity, latency, accuracy, or output format. The range-Doppler images in this publication are formed with a legacy deramp-and-Fourier-transform method (hereafter referred to as the 2D FFT Method) [[Doerry, 1994](#)]. The 2D FFT method has conceptual similarities to the SPECAN algorithm, and was primarily developed for the purpose of quickly processing airborne SAR images (such as the ones produced by SNL's testbed radar). The choice to use the 2D FFT Method is: (1) the 2D FFT Method produces an image in the range-Doppler domain, a convenient format when considering the consumption of the image product by a Kalman filter correcting an inertial navigation system; and (2) the 2D FFT method is perhaps the simplest algorithm to implement and analyze — there is no need for range cell migration correction or data remapping, which are common to the other methods. While any other algorithm could certainly have been used, the 2D FFT method was selected for its simplicity.

2. 2D FFT Image Formation

The following subsection derives the 2D FFT method of range-Doppler image formation using a vertical synthetic aperture radar. This derivation follows the initial derivation provided by Doerry who explored the limitations of some of the approximations invoked below [[Doerry, 1994](#)]. Doerry's derivation stopped short of the full SAR impulse response model which is important for the following navigation analysis, so the full derivation is provided here.

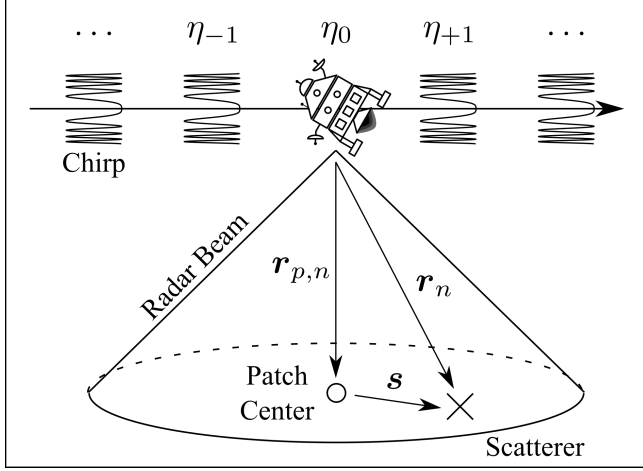


Figure 2: Vertical synthetic aperture radar sensing geometry

Consider the radar sensing geometry shown in Fig. 2. A radar traveling along a straight line emits a series of linear frequency-modulated pulses (chirps). These pulses travel out into the environment, reflect off terrain, and are returned to the radar some time later. It is assumed that the radar system is linear and that the radar's signal is not bounced multiple times between terrain points (the Born approximation). Linearity enables the analysis of the radar system to be reduced to the impulse response analysis of a single point scatterer.

Suppose that the radar emits N equally-spaced chirps between the times $t \in [-(T_a + T_p)/2 + (T_a + T_p)/2]$, where T_a is the approximate synthetic aperture duration and T_p is the chirp pulse envelope duration. Let $\lfloor x \rfloor$ be the integer floor of x . Each chirp is referenced by its respective radar 'slow' time $\eta_n \in \{\eta_{\lfloor -N/2 \rfloor + 1}, \dots, \eta_0, \dots, \eta_{\lfloor N/2 \rfloor}\}$ which is centered on the chirp. The center chirp is defined to be at time $\eta_0 = 0$.

The pulsed chirp signal is modeled as

$$x_{\text{TX}}(t, \eta_n) = A \cdot \cos[2\pi f_0(t - \eta_n) + \pi k(t - \eta_n)^2] \cdot w[(t - \eta_n)/T_p] \cdot w[\eta_n/T_a] \quad (1)$$

where A is the transmitted signal amplitude, f_0 is the radar's center frequency, k is the chirp rate (rate of linear frequency growth), and $w[\tau]$ is a unit rectangle function defined as

$$w[\tau] = \begin{cases} 1 & |\tau| < 0.5 \\ 0 & \text{otherwise} \end{cases} \quad (2)$$

The transmitted signal reflects off a terrain scattering point and returns directly to the radar some time later. Assume that the motion of the radar during the time of flight is negligible. The returned signal is modeled as

$$x_{\text{RX}}(t, \eta_n) = A' \cdot \cos[2\pi f_0(t - \eta_n - 2r_n/c) + \pi k(t - \eta_n - 2r_n/c)^2 + \phi] \cdot w[(t - \eta_n - 2r_n/c)/T_p] \cdot w[\eta_n/T_a] \quad (3)$$

where A' is the returned signal amplitude, $r_n := r[\eta_n]$ is the slow-time-varying range from the radar to the point scatterer, c is the speed of light, and ϕ is a random phase shift induced by the point scatterer.

Let the received signal be mixed with a local replica chirp before quadrature demodulation. The replica chirp is modeled as

$$x_{\text{L}}(t, \eta_n) = \cos[2\pi f_0(t - \eta_n - 2r_{0,n}/c) + \pi k(t - \eta_n - 2r_{0,n}/c)^2] \cdot w[(t - \eta_n - 2r_{0,n}/c)/T'_p] \cdot w[\eta_n/T_a] \quad (4)$$

where $r_{0,n} := r_0[\eta_n]$ is the slow-time-varying range set by the radar (a prior on the approximate range-to-scatterer), and T'_p is the pulse duration of the replica chirp (typically slightly longer than the transmitted chirp). After mixing, low-pass filtering, and

quadrature demodulation, the resulting complex baseband signal is modeled as

$$\begin{aligned} x_{\text{BB}}(t, \eta_n) = & A'' \cdot \exp[-2\pi i k(2r_n/c - 2r_{0,n}/c)(t - \eta_n - 2r_{0,n}/c)] \\ & \cdot \exp[-2\pi i f_0(2r_n/c - 2r_{0,n}/c)] \\ & \cdot \exp[\pi i k(2r_n/c - 2r_{0,n}/c)^2] \\ & \cdot w[(t - \eta_n - 2r_{0,n}/c)/T_p] \cdot w[\eta_n/T_a] \end{aligned} \quad (5)$$

where A'' is a complex constant representing the combined effects of the transmitter's power, antenna gain, path loss, ground reflection coefficients, and receiver losses. Note that a completion of the square is required to obtain Eq. (5).

Suppose now that the baseband signal is sampled in time. Let $t_{m,n} \in \{t_{0,n}, t_{1,n}, \dots, t_{M,n}\}$ be the $M + 1$ radar ‘fast’ time samples centered around the n th chirp and offset by the expected time-of-flight:

$$\begin{aligned} t_{m,n} = & \eta_n + 2r_{0,n}/c + \lfloor m - M/2 \rfloor \Delta t \\ = & \eta_n + 2r_{0,n}/c + \tau_m \end{aligned} \quad (6)$$

where Δt is the fast time sampling period, and τ_m is the m th fast sample time.

Substituting $t = t_{m,n} = \eta_n + 2r_{0,n}/c + \tau_m$ into Eq. (5), the sampled baseband signal is now modeled as

$$\begin{aligned} x_{\text{BB}}(\tau_m, \eta_n) = & A'' \cdot \exp[-2\pi i k(2r_n/c - 2r_{0,n}/c)\tau_m] \\ & \cdot \exp[-2\pi i f_0(2r_n/c - 2r_{0,n}/c)] \\ & \cdot \exp[\pi i k(2r_n/c - 2r_{0,n}/c)^2] \\ & \cdot w[\tau_m/T_p] \cdot w[\eta_n/T_a] \end{aligned} \quad (7)$$

where now the sampled baseband signal is a function of radar fast time τ_m and slow time η_n .

Consider now a local patch region near the point scatterer, as depicted by the base of the cone in Fig. 2. Let $\mathbf{r}_{p,n} := \mathbf{r}_p[\eta_n]$ be the slow-time-varying vector from the radar to the patch center, $\mathbf{r}_n := \mathbf{r}[\eta_n]$ be the slow-time-varying vector from the radar to the point scatterer, and \mathbf{s} be the vector from the patch center to the point scatterer. Then, to the first order, the range to the point scatterer is modeled as

$$\begin{aligned} r_n \simeq & \|\mathbf{r}_{p,n}\| + \hat{\mathbf{r}}_{p,n}^\top \mathbf{s} \\ \simeq & \|\mathbf{r}_{p,n}\| + \Delta r_n \end{aligned} \quad (8)$$

where $\hat{\mathbf{r}}_{p,n}$ is the unit vector of $\mathbf{r}_{p,n}$, and $\Delta r_n := \hat{\mathbf{r}}_{p,n}^\top \mathbf{s}$ is the first-order difference in range between the radar / point scatterer and the radar / patch center. This planar wavefront approximation is appropriate as long as $\|\mathbf{s}\|/\|\mathbf{r}_{p,n}\| \ll 1$.

The range difference Δr_n varies with slow time. The time dependence is made explicit by expanding Δr_n to the first order in slow time about the aperture center time $\eta_0 = 0$:

$$\begin{aligned} \Delta r_n \simeq & \hat{\mathbf{r}}_{p,0}^\top \mathbf{s} + (\dot{\hat{\mathbf{r}}}_{p,0}^\top \mathbf{s})\eta_n \\ \simeq & \Delta r_0 + \Delta \dot{r}_0 \eta_n \end{aligned} \quad (9)$$

where $\Delta r_0 := \hat{\mathbf{r}}_{p,0}^\top \mathbf{s}$ and $\Delta \dot{r}_0 := \dot{\hat{\mathbf{r}}}_{p,0}^\top \mathbf{s}$ are, respectively, the range and range-rate differences of the radar / point scatterer by the radar / patch center at the aperture center time — hereafter referred to as the ‘offset range’ and ‘offset range-rate’.

Substituting Eqs. (8) and (9) into Eq. (7) and choosing the range set by the radar to be equal to the range to the scene center ($r_{0,n} = \|\mathbf{r}_{p,n}\|$), the sampled baseband signal is now modeled as

$$\begin{aligned} x_{\text{BB}}(\tau_m, \eta_n) = & A'' \cdot \exp[-2\pi i k(2(\Delta r_0 + \Delta \dot{r}_0 \eta_n)/c)\tau_m] \\ & \cdot \exp[-2\pi i f_0(2(\Delta r_0 + \Delta \dot{r}_0 \eta_n)/c)] \\ & \cdot \exp[\pi i k(2(\Delta r_0 + \Delta \dot{r}_0 \eta_n)/c)^2] \\ & \cdot w[\tau_m/T_p] \cdot w[\eta_n/T_a] \end{aligned} \quad (10)$$

The goal is to represent the baseband signal in the following form:

$$\begin{aligned} x_{\text{BB}}(\tau_m, \eta_n) &= A''' \cdot \exp[2\pi i f_r \tau_m] \\ &\quad \cdot \exp[2\pi i f_d \eta_n] \\ &\quad \cdot w[\tau_m/T_p] \cdot w[\eta_n/T_a] \end{aligned} \quad (11)$$

where f_r and f_d are, respectively, analogs to the offset range and range-rate. Once in this form, it is clear that the frequency-domain representation of the signal focuses the point scatterer's energy to a sinc pattern at the coordinate pair $[f_r, f_d]$:

$$X_{\text{BB}}(\zeta_m, \xi_n) = A''' \cdot T_p \cdot T_a \cdot \text{sinc}[T_p(\zeta - f_r)] \cdot \text{sinc}[T_a(\xi - f_d)] \quad (12)$$

where $X_{\text{BB}}(\zeta_m, \xi_n)$ is the Fourier Transform of $x_{\text{BB}}(\tau_m, \eta_n)$, ζ_m is the frequency-domain analog of τ_m , ξ_n is the frequency-domain analog of η_n , and the normalized sinc function is defined as

$$\text{sinc}[x] := \frac{\sin[\pi x]}{\pi x} \quad (13)$$

To achieve the signal model form of Eq. (11), two approximations must be invoked. First, the slow time dependence in the first exponential, $\Delta\dot{r}_0\eta_n$, is dropped. This term and its product with fast time τ_m constitute a range walk — a change in the offset range over the aperture collection time. Provided that the imaging standoff distance is large, the aperture collection time is small, and the range resolution is not terribly fine, this term may be safely neglected. Second, the entire third exponential, $\exp[\pi ik(2(\Delta r_0 + \Delta\dot{r}_0\eta_n)/c)^2]$, is assumed to be small and discarded. When viewed through the lens of an eventual Fourier transform, this exponential term acts as a convolution on the slow time data. Provided that the magnitude of the phase change induced by this convolution does not exceed $\pi/4$, it may be safely discarded. Doerry derives explicit limits for this approximation, and the approximation is reasonable provided that the range extent of the reconstructed scene (the range of the range values) is kept small [Doerry, 1994].

Next, constant phase terms are absorbed into A''' , and the sampled baseband signal is modeled as

$$\begin{aligned} x_{\text{BB}}(\tau_m, \eta_n) &= A''' \cdot \exp[2\pi i f_r \tau_m] \\ &\quad \cdot \exp[2\pi i f_d \eta_n] \\ &\quad \cdot w[\tau_m/T_p] \cdot w[\eta_n/T_a] \end{aligned} \quad (14)$$

where

$$f_r = -2k\Delta r_0/c \quad (15)$$

and

$$f_d = -2f_0\Delta\dot{r}_0/c \quad (16)$$

Finally, a two-dimensional Fourier transform registers the point scatterer's energy to the coordinate pair $[f_r, f_d]$. The superposition of focused energy from many point scatterers follows from system linearity. Once registered to $[f_r, f_d]$, scatterers' offset range / range-rate may be recovered using Eqs. (15) and (16). The absolute range / range-rate to point scatterers is recovered by adding the offset range / range-rates to the range / range-rate of the patch center — a known quantity. Finally range-rate \dot{r} is converted to Doppler shift Δf with the following relationship, thus completing the range-Doppler image:

$$\Delta f = 2\frac{f_c}{c}\dot{r} \quad (17)$$

III. INERTIAL NAVIGATION BACKGROUND

The Trusted Inertial Terrain-Aided Navigation algorithm integrates range-Doppler navigation observables extracted from VSAR images into an Inertial Navigation System (INS). The following section provides the necessary background on inertial navigation before the specifics of the TITAN measurements are introduced.

1. INS State Definitions

The TITAN measurements are integrated with standard 15-state inertial navigation system mechanized in the Earth-Centered, Earth-Fixed (ECEF) frame. Measurements from an Inertial Measurement Unit (IMU) drive the INS. The IMU measurements

are modeled as corrupted by a constant bias. The nominal INS state vector captures the kinematic states and IMU biases, and is defined as

$$\mathbf{x} := [\mathbf{p}_{e/b}^{e^\top}, \mathbf{v}_{e/b}^{e^\top}, \mathbf{q}_b^{e^\top}, \mathbf{b}_a^b, \mathbf{b}_g^b]^\top \quad (18)$$

where $\mathbf{p}_{e/b}^e \in \mathbb{R}^3$ and $\mathbf{v}_{e/b}^e \in \mathbb{R}^3$ are, respectively, the position and velocity of the IMU in the ECEF frame, $\mathbf{q}_b^e \in \mathbb{R}^4$ is an arbitrary quaternion representation of $\mathbf{R}_b^e \in \text{SO}(3)$, a rotation matrix that transforms a vector expressed in the IMU body frame to a vector expressed in the ECEF frame, and $\mathbf{b}_a^b \in \mathbb{R}^3$ and $\mathbf{b}_g^b \in \mathbb{R}^3$ are, respectively, the accelerometer and gyroscope biases in the IMU body frame.

The INS also models its error state:

$$\delta\mathbf{x} := [\delta\mathbf{p}_{e/b}^{e^\top}, \delta\mathbf{v}_{e/b}^{e^\top}, \delta\boldsymbol{\theta}^e, \delta\mathbf{b}_a^b, \delta\mathbf{b}_g^b]^\top \quad (19)$$

where δ indicates an error state, and $\delta\boldsymbol{\theta}^e \in \mathbb{R}^3$ is a small-angle error mechanized in the ECEF frame.

The true, nominal, and error states are related as

$$\mathbf{p}_{e/b}^{e,*} = \mathbf{p}_{e/b}^e + \delta\mathbf{p}_{e/b}^e \quad (20)$$

$$\mathbf{v}_{e/b}^{e,*} = \mathbf{v}_{e/b}^e + \delta\mathbf{v}_{e/b}^e \quad (21)$$

$$\mathbf{R}_b^{e,*} = (\mathbf{I}_{3 \times 3} - [\delta\boldsymbol{\theta}^e \wedge]) \cdot \mathbf{R}_b^e \quad (22)$$

$$\mathbf{b}_a^{b,*} = \mathbf{b}_a^b + \delta\mathbf{b}_a^b \quad (23)$$

$$\mathbf{b}_g^{b,*} = \mathbf{b}_g^b + \delta\mathbf{b}_g^b \quad (24)$$

where asterisks indicate the true states and where $[\delta\boldsymbol{\theta}^e \wedge]$ is the cross product matrix formed from $\delta\boldsymbol{\theta}^e$.

2. INS Nominal State Dynamics

The continuous-time dynamics of the nominal navigation states are modeled as [Groves, 2013]

$$\dot{\mathbf{p}}_{e/b}^e = \mathbf{v}_{e/b}^e \quad (25)$$

$$\dot{\mathbf{v}}_{e/b}^e = \mathbf{a}_{e/b}^{e,*} \quad (26)$$

$$\dot{\mathbf{R}}_b^e = \mathbf{R}_b^e \cdot \boldsymbol{\Omega}_{i/b}^{b,*} - \boldsymbol{\Omega}_{i/e}^e \cdot \mathbf{R}_b^e \quad (27)$$

$$\dot{\mathbf{b}}_a^b = \mathbf{0} \quad (28)$$

$$\dot{\mathbf{b}}_g^b = \mathbf{0} \quad (29)$$

where $\mathbf{a}_{e/b}^{e,*} \in \mathbb{R}^3$ is the true acceleration of the body away from the ECEF frame, $\boldsymbol{\Omega} := [\boldsymbol{\omega} \wedge]$ is the skew-symmetric matrix formed from $\boldsymbol{\omega} \in \mathbb{R}^3$ and inherits the sub- and superscripts from $\boldsymbol{\omega}$, $\boldsymbol{\omega}_{i/b}^{b,*} \in \mathbb{R}^3$ is true rotation rate vector of the IMU away from the Earth-Centered Inertial (ECI) frame, and $\boldsymbol{\omega}_{i/e}^e \in \mathbb{R}^3$ is the rotation rate vector of the ECEF frame away from the ECI frame. The true ECEF acceleration and inertial angular rate vectors, $\mathbf{a}_{e/b}^{e,*}$ and $\boldsymbol{\omega}_{i/b}^{b,*}$ respectively, are derived from IMU measurements.

IMU measurements replace the dynamics model for the position, velocity, and attitude of the navigation system. The IMU is modeled as a triad of orthogonal accelerometers and gyroscopes that measure the vector specific force and inertial angular rate. The IMU's measurements are modeled as corrupted by a constant bias and additive, independent, zero-mean Gaussian noise. The accelerometer specific force measurements are modeled as:

$$\mathbf{f}_{i/b}^b = \mathbf{f}_{i/b}^{b,*} - \mathbf{b}_a^b - \boldsymbol{\epsilon}_a^b \quad (30)$$

where $\mathbf{f}_{i/b}^b \in \mathbb{R}^3$ and $\mathbf{f}_{i/b}^{b,*} \in \mathbb{R}^3$ are, respectively, the measured and true specific force vectors, $\mathbf{b}_a^b \in \mathbb{R}^3$ is a constant bias, and $\boldsymbol{\epsilon}_a^b \in \mathbb{R}^3$ is Gaussian noise with covariance $\mathbf{Q}_a \in \mathbb{R}^{3 \times 3}$. The specific force is related to the ECEF acceleration, gravitation, centrifugal, and Coriolis forces as [Groves, 2013]:

$$\mathbf{a}_{e/b}^{e,*} = \mathbf{R}_b^e \mathbf{f}_{i/b}^{b,*} + \mathbf{g}^e - \boldsymbol{\Omega}_{i/e}^e \cdot \boldsymbol{\Omega}_{i/e}^e \cdot \mathbf{p}_{e/b}^e - 2\boldsymbol{\Omega}_{i/e}^e \cdot \mathbf{v}_{e/b}^e \quad (31)$$

where $\mathbf{g}^e \in \mathbb{R}^3$ is the gravitation of the sensor.

Similarly, the gyroscope measurements are modeled as

$$\omega_{i/b}^b = \omega_{i/b}^{b,*} - \mathbf{b}_g^b - \boldsymbol{\epsilon}_g^b \quad (32)$$

where $\omega_{i/b}^b \in \mathbb{R}^3$ and $\omega_{i/b}^{b,*} \in \mathbb{R}^3$ are, respectively, the measured and true angular rates of the sensor away from the inertial frame, $\mathbf{b}_g^b \in \mathbb{R}^3$ is a constant bias, and $\boldsymbol{\epsilon}_g^b \in \mathbb{R}^3$ is Gaussian noise with covariance $\mathbf{Q}_g \in \mathbb{R}^{3 \times 3}$.

Substituting the IMU models in Eqs. (30), (31), and (32) into the dynamics model in Eqs. (25) - (27) produces the following IMU-driven dynamics model:

$$\dot{\mathbf{p}}_{e/b}^e = \mathbf{v}_{e/b}^e \quad (33)$$

$$\dot{\mathbf{v}}_{e/b}^e = \mathbf{R}_b^e(\mathbf{f}_{i/b}^b + \mathbf{b}_a^b + \boldsymbol{\epsilon}_a^b) + \mathbf{g}^e - \boldsymbol{\Omega}_{i/e}^e \cdot \boldsymbol{\Omega}_{i/e}^e \cdot \mathbf{p}_{e/b}^e - 2\boldsymbol{\Omega}_{i/e}^e \cdot \mathbf{v}_{e/b}^e \quad (34)$$

$$\dot{\mathbf{R}}_b^e = \mathbf{R}_b^e \cdot [(\omega_{i/b}^b + \mathbf{b}_g^b + \boldsymbol{\epsilon}_g^b) \wedge] - \boldsymbol{\Omega}_{i/e}^e \cdot \mathbf{R}_b^e \quad (35)$$

The nominal system dynamics are discretized under the assumption that the noise is zero, the propagation interval is small, and second-and higher-order error terms are negligible. From [Groves, 2013], the *precision* nominal discrete-time propagation equations from a prior period $[-]$ to a posterior period $[+]$ over an interval Δt given a gyroscope measurement $\omega_{i/b}^b$ and accelerometer measurement $\mathbf{f}_{i/b}^b$ are the following. First, propagate the accelerometer and gyroscope biases (they are constant):

$$\mathbf{b}_a^b[+] = \mathbf{b}_a^b[-] \quad (36)$$

$$\mathbf{b}_g^b[+] = \mathbf{b}_g^b[-] \quad (37)$$

Then, correct the IMU biases:

$$\bar{\mathbf{f}}_{i/b}^b = \mathbf{f}_{i/b}^b + \mathbf{b}_a^b[+] \quad (38)$$

$$\bar{\omega}_{i/b}^b = \omega_{i/b}^b + \mathbf{b}_g^b[+] \quad (39)$$

Next, propagate the attitude:

$$\bar{\boldsymbol{\alpha}}_{i/b}^b = \bar{\omega}_{i/b}^b \Delta t \quad (40)$$

$$\mathbf{R}_{b+}^{b-} = \exp[\bar{\boldsymbol{\alpha}}_{i/b}^b \wedge] \quad (41)$$

$$\mathbf{R}_b^e[+] = \mathbf{R}_b^e[-] \cdot \mathbf{R}_{b+}^{b-} - \boldsymbol{\Omega}_{i/e}^e \cdot \mathbf{R}_b^e[-] \Delta t \quad (42)$$

Then, correct any ‘smearing’ of the sensed specific force vector due to the rotation of the sensor over the IMU integration interval:

$$\mathbf{R}_{\bar{b}}^{b-} = \mathbf{I}_3 + (1 - \cos |\bar{\boldsymbol{\alpha}}_{i/b}^b|) \frac{[\bar{\boldsymbol{\alpha}}_{i/b}^b \wedge]}{|\bar{\boldsymbol{\alpha}}_{i/b}^b|^2} + (1 - \frac{\sin |\bar{\boldsymbol{\alpha}}_{i/b}^b|}{|\bar{\boldsymbol{\alpha}}_{i/b}^b|}) \frac{[\bar{\boldsymbol{\alpha}}_{i/b}^b \wedge]^2}{|\bar{\boldsymbol{\alpha}}_{i/b}^b|^2} \quad (43)$$

$$\bar{\mathbf{R}}_b^e = \mathbf{R}_b^e[-] \cdot \mathbf{R}_{\bar{b}}^{b-} - \frac{1}{2} \boldsymbol{\Omega}_{i/e}^e \cdot \mathbf{R}_b^e[-] \Delta t \quad (44)$$

$$\bar{\mathbf{f}}_{i/b}^e = \bar{\mathbf{R}}_b^e \cdot \bar{\mathbf{f}}_{i/b}^b \quad (45)$$

Finally, calculate the ECEF acceleration, and propagate the velocity and position:

$$\bar{\mathbf{a}}_{e/b}^e = \bar{\mathbf{f}}_{i/b}^e + \mathbf{g}^e - \boldsymbol{\Omega}_{i/e}^e \cdot \boldsymbol{\Omega}_{i/e}^e \cdot \mathbf{p}_{e/b}^e[-] - 2\boldsymbol{\Omega}_{i/e}^e \cdot \mathbf{v}_{e/b}^e[-] \quad (46)$$

$$\mathbf{v}_{e/b}^e[+] = \mathbf{v}_{e/b}^e[-] + \bar{\mathbf{a}}_{e/b}^e \Delta t \quad (47)$$

$$\mathbf{p}_{e/b}^e[+] = \mathbf{p}_{e/b}^e[-] + \frac{1}{2} (\mathbf{v}_{e/b}^e[+] + \mathbf{v}_{e/b}^e[-]) \Delta t \quad (48)$$

3. INS Error State Dynamics

The error state $\delta\mathbf{x}$ is modeled as a stochastic, zero-mean, multivariate Gaussian random variable that evolves in time according to the following linear, white noise system:

$$\delta\dot{\mathbf{x}} = \mathbf{F} \cdot \delta\mathbf{x} + \mathbf{G} \cdot \begin{bmatrix} \epsilon_a \\ \epsilon_g \end{bmatrix} \quad (49)$$

where $\mathbf{F} \in \mathbb{R}^{15 \times 15}$ is the continuous-time error state transition matrix, $\mathbf{G} \in \mathbb{R}^{15 \times 6}$ is the white noise mapping matrix, and $\epsilon_a \in \mathbb{R}^3$ and $\epsilon_g \in \mathbb{R}^3$ are, respectively, accelerometer and gyroscope white noise samples with corresponding power spectral densities $S_a \mathbf{I}_{3 \times 3}$ and $S_g \mathbf{I}_{3 \times 3}$.

The linear, white noise dynamics in Eq. (49) and assumption of a zero-mean Gaussian prior ensure that error state maintains its Gaussian distribution. The distribution is then completely characterized by its mean and covariance. Let $\delta\mathbf{x}_k \in \mathbb{R}^{15}$ and $\mathbf{P}_k \in \mathbb{R}^{15 \times 15}$ be the error state mean and covariance at time t_k . The discrete-time solution to the error state dynamics from t_k to t_{k+1} over a period Δt is [Groves, 2013]

$$\delta\mathbf{x}_{k+1} = 0 \quad (50)$$

$$\mathbf{P}_{k+1} = \mathbf{F}_d \cdot \mathbf{P}_k \cdot \mathbf{F}_d^\top + \mathbf{Q}_d \quad (51)$$

where \mathbf{F}_d is the discrete-time error state transition matrix approximated by

$$\mathbf{F}_d = \mathbf{I}_{15 \times 15} + \mathbf{F} \Delta t + \frac{1}{2} \mathbf{F} \Delta t^2 \quad (52)$$

and \mathbf{Q}_d is the discrete-time process noise covariance matrix approximated by

$$\mathbf{Q}_d = \mathbf{G} \begin{bmatrix} S_a \mathbf{I}_{3 \times 3} & \mathbf{0}_{3 \times 3} \\ \mathbf{0}_{3 \times 3} & S_g \mathbf{I}_{3 \times 3} \end{bmatrix} \mathbf{G}^\top \Delta t \quad (53)$$

The matrices \mathbf{F} and \mathbf{G} are [Groves, 2013]

$$\mathbf{F} = \begin{bmatrix} \mathbf{0}_{3 \times 3} & \mathbf{F}_{12} & \mathbf{0}_{3 \times 3} & \mathbf{0}_{3 \times 3} & \mathbf{0}_{3 \times 3} \\ \mathbf{F}_{21} & \mathbf{F}_{22} & \mathbf{F}_{23} & \mathbf{F}_{24} & \mathbf{0}_{3 \times 3} \\ \mathbf{0}_{3 \times 3} & \mathbf{0}_{3 \times 3} & \mathbf{F}_{33} & \mathbf{0}_{3 \times 3} & \mathbf{F}_{35} \\ \mathbf{0}_{3 \times 3} & \mathbf{0}_{3 \times 3} & \mathbf{0}_{3 \times 3} & \mathbf{0}_{3 \times 3} & \mathbf{0}_{3 \times 3} \\ \mathbf{0}_{3 \times 3} & \mathbf{0}_{3 \times 3} & \mathbf{0}_{3 \times 3} & \mathbf{0}_{3 \times 3} & \mathbf{0}_{3 \times 3} \end{bmatrix} \quad (54)$$

where

$$\mathbf{F}_{12} = \mathbf{I}_{3 \times 3} \quad (55)$$

$$\mathbf{F}_{21} = \frac{\partial \mathbf{g}^e}{\partial \mathbf{p}_{e/b}^e} - \boldsymbol{\Omega}_{i/e}^e \cdot \boldsymbol{\Omega}_{i/e}^e \quad (56)$$

$$\mathbf{F}_{22} = -2\boldsymbol{\Omega}_{i/e}^e \quad (57)$$

$$\mathbf{F}_{23} = -[\mathbf{R}_b^e (\mathbf{f}_{i/b}^b + \mathbf{b}_a^b) \wedge] \quad (58)$$

$$\mathbf{F}_{24} = \mathbf{R}_b^e \quad (59)$$

$$\mathbf{F}_{33} = -\boldsymbol{\Omega}_{i/e}^e \quad (60)$$

$$\mathbf{F}_{35} = \mathbf{R}_b^e \quad (61)$$

where $\frac{\partial \mathbf{g}^e}{\partial \mathbf{p}_{e/b}^e}$ is the partial derivative of the gravitational model by the position and evaluated at the current position estimate.

The white noise mapping matrix is [Groves, 2013]

$$\mathbf{G} = \begin{bmatrix} \mathbf{0}_{3 \times 3} & \mathbf{0}_{3 \times 3} \\ \mathbf{R}_b^e & \mathbf{0}_{3 \times 3} \\ \mathbf{0}_{3 \times 3} & \mathbf{R}_b^e \\ \mathbf{0}_{3 \times 3} & \mathbf{0}_{3 \times 3} \\ \mathbf{0}_{3 \times 3} & \mathbf{0}_{3 \times 3} \end{bmatrix} \quad (62)$$

4. INS Measurement Correction

Suppose that at time t_k a sensor produces a measurement of the INS state vector (e.g., GPS, radar, visual, etc.). Let $\mathbf{z}_k \in \mathbb{R}^L$ be the realized measurement, and suppose it is modeled as

$$\mathbf{z}_k = \mathbf{h}(\mathbf{x}_k^*) + \mathbf{w}_k \quad (63)$$

where $\mathbf{h}(\mathbf{x}_k^*) : \mathbb{R}^{16} \rightarrow \mathbb{R}^L$ is the modeled measurement function, $\mathbf{x}_k^* \in \mathbb{R}^{16}$ is the true state, and $\mathbf{w}_k \in \mathbb{R}^L$ is random noise sampled from an independent, zero-mean Gaussian distribution with covariance $\mathbf{R}_k \in \mathbb{R}^{L \times L}$. Let this measurement model be linearized about the error state prior $\delta\bar{\mathbf{x}}_k \sim \mathcal{N}(\mathbf{0}, \bar{\mathbf{P}}_k)$. After invoking the relationship between the true, nominal, and error states in Eqs. (20) - (24), the measurement model becomes a linear function of the error state:

$$\underbrace{\mathbf{z}_k - \mathbf{h}(\mathbf{x}_k)}_{\mathbf{y}} \simeq \mathbf{H}_k \cdot \delta\mathbf{x}_k + \mathbf{w}_k \quad (64)$$

where $\mathbf{H}_k \in \mathbb{R}^{L \times 15}$ is the error state measurement matrix.

Then a posterior estimate of the error state $\delta\hat{\mathbf{x}}_k \sim \mathcal{N}(\delta\hat{\mathbf{x}}_k, \hat{\mathbf{P}}_k)$ may be formed with the following set of Kalman equations:

$$\mathbf{S}_k = \mathbf{H}_k \cdot \bar{\mathbf{P}}_k \cdot \mathbf{H}_k^\top + \mathbf{R}_k \quad (65)$$

$$\mathbf{K}_k = \bar{\mathbf{P}}_k \cdot \mathbf{H}_k^\top \cdot \mathbf{S}_k^{-1} \quad (66)$$

$$\delta\hat{\mathbf{x}}_k = \mathbf{K}_k \cdot (\mathbf{z}_k - \mathbf{h}(\mathbf{x}_k)) \quad (67)$$

$$\hat{\mathbf{P}}_k = (\mathbf{I} - \mathbf{K}_k \cdot \mathbf{H}_k) \cdot \bar{\mathbf{P}}_k \cdot (\mathbf{I} - \mathbf{K}_k \cdot \mathbf{H}_k)^\top + \mathbf{K}_k \cdot \mathbf{R}_k \cdot \mathbf{K}_k^\top \quad (68)$$

Once a posterior estimate of the error state is formed, the nominal state and error state are composed with Eqs. (20) - (24) to ‘correct’ the nominal state. This final reset step completes the Kalman update and ensures that the zero-mean error state assumptions are appropriately reset.

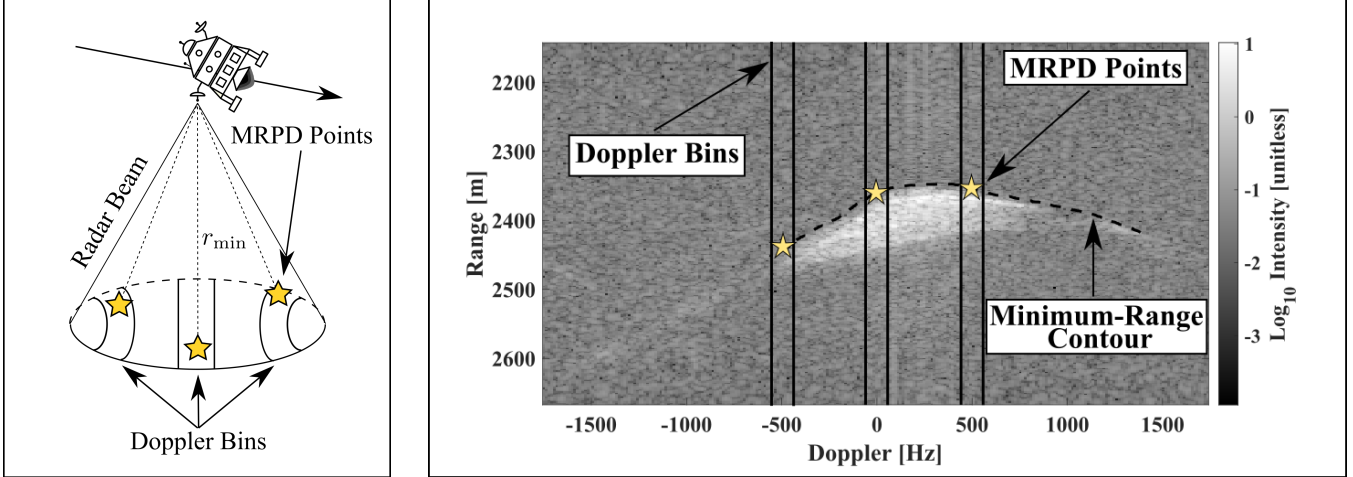
IV. TRUSTED INERTIAL TERRAIN-AIDED NAVIGATION

The following section introduces the Trusted Inertial Terrain-Aided Navigation algorithm. TITAN is named to specifically hearken back to the Sandia Inertial Terrain-Aided Navigation (SITAN) algorithm with which it shares conceptual similarities and origins. Similar to how the SITAN algorithm integrated scalar ground clearance measurements derived from a radar altimeter into an Extended Kalman Filter (EKF), the TITAN algorithm integrates vector range-Doppler measurements derived from a VSAR into a Extended Kalman Filter. In both instances, the radar measurements are ‘correlated’ against a local digital terrain elevation model (DEM) as part of the EKF update, wherein realized radar measurements are differenced by radar measurements predicted from the radar’s prior state estimate and a DEM. The word ‘trusted’ is included in the algorithm name as it is intended that the vector range-Doppler measurements will be cross-validated against one another to improve the ultimate navigation accuracy and engender trust in the algorithm.

The following subsections describe the key components of the TITAN algorithm. First, the TITAN measurement is defined in Cartesian navigation, radar measurement, and mathematical domains. Then, the process of detecting and extracting the TITAN measurement from a VSAR image is provided. Next, steps to predict the TITAN measurement from a prior state estimate and DEM are described. Finally, a finite-difference approach to calculating the measurement Jacobian is suggested.

1. Measurement Definition

The TITAN algorithm operates on a set of minimum-range, prescribed-Doppler (MRPD) measurements. An MRPD measurement is defined as first detected range within a set of terrain scatter points whose Doppler shifts lie within a prescribed range of values (a Doppler bin). Understand that while the following images only depict three MRPD measurements, the TITAN algorithm is not limited to a three-vector measurement and that an arbitrary number of MRPD measurements may be used at any measurement epoch.



(a) Three MRPD measurements are prescribed in the Cartesian domain — aft, nadir, and fore the radar.

(b) Three MRPD measurements are prescribed in the radar domain — centered at -500 Hz, 0 Hz, and +500 Hz.

Figure 3: Three MRPD measurements viewed in the Cartesian & radar domains.

Fig. 3 illustrates three MRPD measurements as viewed in the Cartesian navigation domain (left) and the radar measurement domain (right). In the Cartesian domain, a radar flies along a straight line and images an elliptical ground patch. The TITAN algorithm has prescribed three Doppler bins — aft, nadir, and fore the radar. Each Doppler bin occupies a narrow rectilinear region on the ground that spans the cross-track extent of the radar’s beam width. The MRPD measurement vector is the range (dotted line) to the closest ground point (yellow star) in each of the three Doppler bins. In the radar domain, the radar forms a range-Doppler image. The TITAN algorithm prescribes three Doppler bins centered at -500 Hz, 0 Hz, and +500 Hz that span several image columns. The three MRPD measurements lie at the intersection of the minimum range contour — set of first detections for every Doppler offset (image column) — and the three prescribed Doppler bins, and are indicated by yellow stars.

Now, the mathematical definition. Let the position, velocity, and attitude components of the inertial navigator’s state be transformed into the same frame that local map data is expressed in. The local map frame vector is defined as

$$\boldsymbol{x}^\ell := [\boldsymbol{p}_{\ell/r}^{\ell\top}, \boldsymbol{v}_{\ell/r}^{\ell\top}, \boldsymbol{q}_r^\ell]^\top \quad (69)$$

where $\boldsymbol{p}_{\ell/r}^\ell \in \mathbb{R}^3$ and $\boldsymbol{v}_{\ell/r}^\ell \in \mathbb{R}^3$ are, respectively, the position and velocity of the radar in a local map frame, and $\boldsymbol{q}_r^\ell \in \mathbb{R}^4$ is an arbitrary quaternion representation of $\boldsymbol{R}_r^\ell \in \text{SO}(3)$, a rotation matrix that transforms a vector expressed in the radar frame to a vector expressed in the local map frame. The TITAN measurement function that maps the state vector \boldsymbol{x}^ℓ to N MRND measurements is defined as

$$\boldsymbol{h}[\boldsymbol{x}^\ell, \boldsymbol{\theta}] := [h_{(1)}[\boldsymbol{x}^\ell, \boldsymbol{\theta}_{(1)}], h_{(2)}[\boldsymbol{x}^\ell, \boldsymbol{\theta}_{(2)}], \dots, h_{(N)}[\boldsymbol{x}^\ell, \boldsymbol{\theta}_{(N)}]]^\top \quad (70)$$

$$h_{(n)}[\boldsymbol{x}^\ell, \boldsymbol{\theta}_{(n)}] := \min_{\boldsymbol{p}_{\ell/r}^\ell \in \mathcal{G}[\boldsymbol{x}^\ell, \boldsymbol{\theta}_{(n)}]} \|\boldsymbol{p}_{\ell/p}^\ell - \boldsymbol{p}_{\ell/r}^\ell\| \quad (71)$$

where $\boldsymbol{p}_{\ell/p}^\ell$ is the position of a ground point in the local map frame, $\boldsymbol{\theta} := [\boldsymbol{\theta}_{(1)}^\top, \boldsymbol{\theta}_{(2)}^\top, \dots, \boldsymbol{\theta}_{(N)}^\top]^\top$ is a parameter vector that defines the N prescribed Doppler bins, $h_{(n)}[\boldsymbol{x}, \boldsymbol{\theta}_{(n)}]$ is the scalar measurement function that maps the radar’s state vector to the MRPD range measurement associated with the n th Doppler bin, and $\mathcal{G}[\boldsymbol{x}, \boldsymbol{\theta}_{(n)}]$ is the set of points on the ground that are (1) contained within the radar’s beam width, and (2) contained within the n th prescribed Doppler bin.

Let the radar frame be defined as z along the radar’s boresight vector (primarily pointed down), x aligned with the flight direction and orthogonal to z , and y completing an orthogonal triad. A ground point is determined to be within a radar’s beam width (assumed elliptical cone) if it satisfies the following criterion:

$$\left(\frac{\Delta x^r}{\Delta z^r \tan[\phi_x/2]} \right)^2 + \left(\frac{\Delta y^r}{\Delta z^r \tan[\phi_y/2]} \right)^2 \leq 1 \quad (72)$$

where Δx^r , Δy^r , and Δz^r are, x, y, and z components of $\Delta p^r := \mathbf{R}_r^{\ell^\top} \cdot (\mathbf{p}_{\ell/p}^\ell - \mathbf{p}_{\ell/r}^\ell)$, the vector from the radar to the ground point expressed in the radar frame, and where ϕ_x and ϕ_y are, respectively, the radar beam widths in the radar x and y directions. Generally, ϕ_x and ϕ_y are referred to as the along-track and cross-track beam widths.

A ground point is determined to lie within the n th Doppler bin if

$$\Delta f_{(n,-)} \leq \Delta f < \Delta f_{(n,+)} \quad (73)$$

where Δf is the ground point's Doppler shift, and where $\Delta f_{(n,-)}$ and $\Delta f_{(n,+)}$ are, respectively, the prescribed lower and upper bounds of the n th Doppler bin. Note that the radar Doppler shift is twice the Doppler shift used in GNSS due to reflected ranging:

$$\Delta f = 2 \frac{f_c}{c} \mathbf{v}_{\ell/r}^{\ell^\top} \left(\frac{\mathbf{p}_{\ell/p}^\ell - \mathbf{p}_{\ell/r}^\ell}{\|\mathbf{p}_{\ell/p}^\ell - \mathbf{p}_{\ell/r}^\ell\|} \right) \quad (74)$$

where f_c is the radar's center frequency and c is the speed of light.

Together, Eqs. (70), (71), (72), and (73) fully define the TITAN measurement.

2. Measurement Detection

Suppose that a VSAR produces a range-Doppler image like the one in Fig. 1. TITAN MRPD measurements are extracted from the range-Doppler image by determining the first return in the prescribed Doppler bins. A simple threshold is set at 8 times the median VSAR image intensity. The first return for every prescribed Doppler bin is determined as the range at which the intensity return first exceeds this threshold.

The number of ‘noise’ pixels in radar images such as Fig. 1 far exceeds the number of ‘signal’ pixels. Given this dominance, the median image magnitude effectively represents the average noise value in an image. The 8x median sets the threshold value approximately 9 dB higher than the average noise value. Constant detection thresholds set at values different than 8x median were experimented with — they generally traded off more sensitive detections for higher false alarm rates. Ultimately the 8x median threshold was set because it worked well enough over a range of images, but future work should consider an adaptive detection threshold conditioned on identified noise regions in VSAR images.

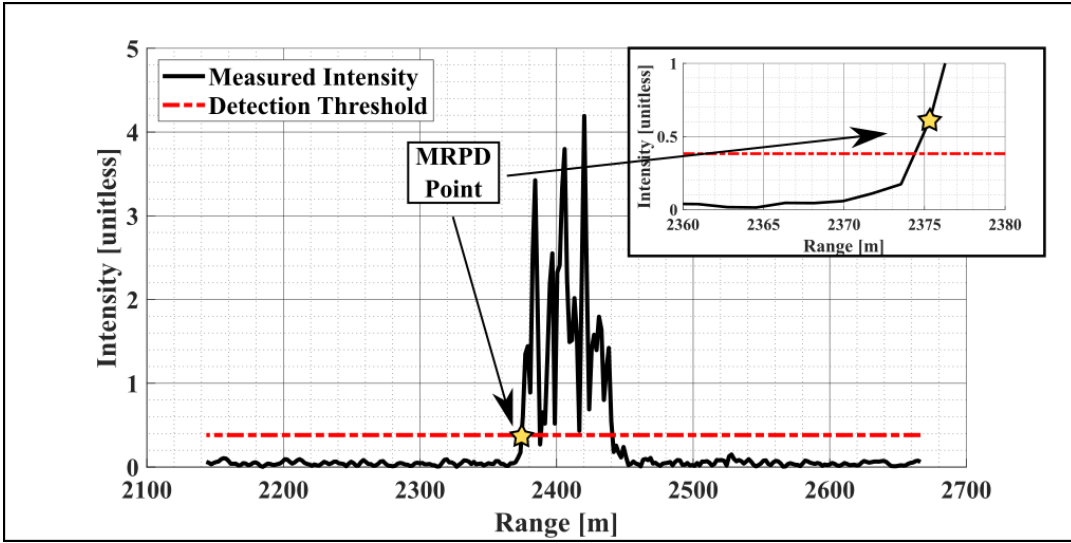


Figure 4: Range-Doppler intensity curve in the zero-Doppler bin, and a threshold set at 8 times the median image intensity.

Fig. 4 plots the image intensity and detection threshold for the zero-Doppler bin of Fig. 1. The minimum range was detected by the threshold operation at 2375.34 meters. The subplot in the top right corner magnifies the nearby detection area. From this magnified plot, one might determine a better MRPD detection to be at approximately 2373 meters where the intensity curve begins to rapidly increase. Errors in the detection algorithm (perhaps such as this) manifest as errors in the range measurements, which degrade the subsequent navigation correction. Future work on adaptive detection thresholds will quantify the effects of these errors on the navigation solution.

3. Measurement Prediction

The following subsection describes how to predict a TITAN measurement given prior information of a radar's position, velocity, attitude, and relevant radar parameters. While, Eqs. (70), (71), (72), and (73) define the TITAN measurement function, the following subsection describes how to simulate it.

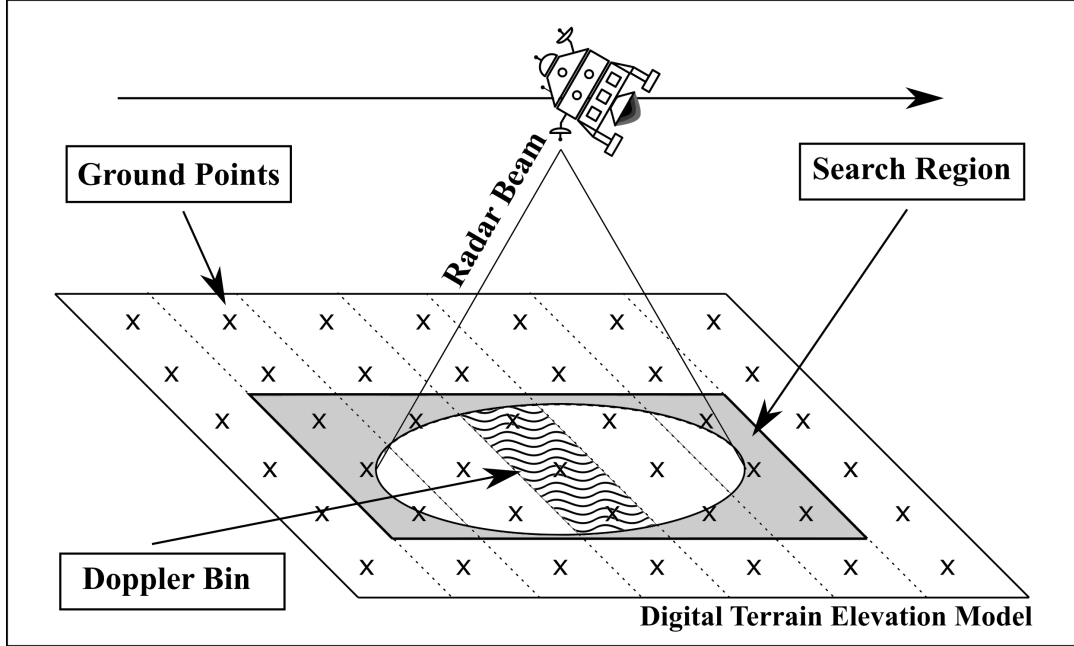


Figure 5: Visualization of the five-step TITAN measurement function.

Fig. 5 illustrates the five-step process used to predict and simulate the TITAN measurements. Given prior information of a radar's position, velocity, and attitude; information about the radar's center frequency, beam width, and Doppler bin extents; and a digital terrain elevation model, perform the following:

1. Establish a search region within the DEM that inscribes the radar's ground-projected beam width (grey rectangle).
2. Filter out any of the inscribed points that do not meet the beam width criterion from Eq. (72) (results in ellipse).
3. Evaluate the Doppler shift to the beam-width-filtered points.
4. For every Doppler bin, filter out the beam-width-filtered points whose Doppler shifts do not meet the Doppler bin criterion from Eq. (73) (results in wavy region for one Doppler bin).
5. Evaluate the range to the Doppler-shift-filtered points and select the minimum.

This five-step prediction process is formalized in pseudocode in Algorithm 1:

Algorithm 1: TITANMeasurementPrediction

Input : $\mathbf{p}_{\ell/r}^\ell, \mathbf{v}_{\ell/r}^\ell, \mathbf{R}_r^\ell, \theta, N$

Output : \mathbf{z}

- 1 $\mathbf{p}_{\ell/p,1:j}^\ell = \text{EstablishSearchRegion}(\mathbf{p}_{\ell/r}^\ell, \mathbf{R}_r^\ell, \theta)$
 - 2 $\mathbf{p}_{\ell/p,1:k}^\ell = \text{BeamWidthMask}(\mathbf{p}_{\ell/r}^\ell, \mathbf{p}_{\ell/p,1:j}^\ell, \mathbf{R}_r^\ell, \theta)$
 - 3 $\Delta \mathbf{f}_{1:k} = \text{EvaluateDoppler}(\mathbf{p}_{\ell/r}^\ell, \mathbf{p}_{\ell/p,1:k}^\ell, \mathbf{v}_{\ell/r}^\ell, \theta,)$
 - 4 **for** $i = 1:N$ **do**
 - 5 $\mathbf{p}_{\ell/p,1:m}^\ell = \text{DopplerBinMask}(\mathbf{p}_{\ell/p,1:k}^\ell, \Delta \mathbf{f}_{1:k}, \theta_{(i)})$
 - 6 $\mathbf{z}_i = \text{EvaluateMinRange}(\mathbf{p}_{\ell/r}^\ell, \mathbf{p}_{\ell/p,1:m}^\ell)$
 - 7 **end**
-

The output of this five-step prediction process is a vector of predicted MRPD measurements.

4. Measurement Jacobian

The Extended Kalman Filter requires a matrix $\mathbf{H} \in \mathbb{R}^{L \times 15}$ that linearly maps a navigator's error state to the measurement residuals. In many cases, \mathbf{H} is determined by differentiating the measurement function by the error state vector and evaluating it at the navigator's current state. In the case of TITAN, it is not straightforward to apply a partial derivative to the measurement function given by Eqs. (70), (71), (72), and (73) as together they define a *constrained nonlinear optimization problem*. In cases such as this where a partial derivative is difficult, a finite-difference approximation of \mathbf{H} is often invoked:

$$\mathbf{H}^{(i)} \simeq \frac{\mathbf{h}(\mathbf{x} + \delta \mathbf{x}^{(i)}) - \mathbf{h}(\mathbf{x} - \delta \mathbf{x}^{(i)})}{2\|\delta \mathbf{x}^{(i)}\|} \quad (75)$$

where $\mathbf{H}^{(i)} \in \mathbb{R}^L$ is the i th column of \mathbf{H} and $\delta \mathbf{x}^{(i)} \in \mathbb{R}^N$ is a perturbation vector that is zero everywhere except the i th component.

A finite-difference method based on the Cubature Transform is suggested instead of the approach in Eq. (75). The Cubature Transform is a sampling-based method closely related to the Unscented Transform that is very effective at capturing higher-order effects of non-linear transforms [Arasaratnam and Haykin, 2009]. The Cubature Transform empirically evaluates the error state / innovation cross-covariance matrix $\mathbf{P}_{xy} \in \mathbb{R}^{15 \times L}$ and innovation covariance matrix $\mathbf{P}_{yy} \in \mathbb{R}^{L \times L}$ by (1) sampling the state vector 30 times, (2) perturbing state the samples, (3) evaluating the measurement function with the perturbed states samples, and (4) empirically calculating the resulting data spread. Normally, the product of these Cubature Transform matrices is used to form the Cubature Kalman gain matrix $\mathbf{K} \in \mathbb{R}^{15 \times L}$:

$$\mathbf{K} = \mathbf{P}_{xy} \cdot \mathbf{P}_{yy}^{-1} \quad (76)$$

When compared to the extended Kalman filter equation for the Kalman gain

$$\mathbf{K} = (\mathbf{P} \cdot \mathbf{H}^\top) \cdot \mathbf{S}^{-1} \quad (77)$$

where $\mathbf{P} \in \mathbb{R}^{15 \times 15}$ is the prior error state covariance matrix and $\mathbf{S} \in \mathbb{R}^{L \times L}$ is the EKF innovations covariance, it is clear that one could approximate the \mathbf{H} matrix as

$$\mathbf{H} \simeq (\mathbf{P}^{-1} \cdot \mathbf{P}_{xy})^\top \quad (78)$$

This process of approximating the \mathbf{H} matrix is similar to what Yoder et al. did with the Unscented Transform in their tightly-coupled GNSS publication [Yoder and Humphreys, 2023]. Note that the Cubature Transform could have been used to perform the entire Kalman update, circumventing the EKF update. In the case of this publication and its supporting software, the EKF software already existed and so the measurement function was adjusted to fit the navigator instead of the navigator to the measurement function. Future work might consider the performance difference between this EKF-from-Cubature-Transform update and a standard Cubature Transform update.

The measurement function is not directly sensitive to all error states, and so a large portion of \mathbf{H} will be zero. Given the sampling nature of the Cubature Transform, some computation may be saved by only sampling the states the measurement function is sensitive to — namely, position and velocity. Technically, the measurement function could be sensitive to attitude

errors, though they are often very small and their effect on the measurement function is indirect at best: small attitude errors change which ground points are illuminated by the radar at the edges of the beam width. As long as the radar beam width is large enough that the closest-range points are not at the edges of the beam width, the effect of attitude errors may be safely discarded.

Let $\tilde{\mathbf{H}} \in \mathbb{R}^{L \times 6}$ be the measurement matrix recovered by sampling over only the position and velocity states. Then the total measurement matrix is given by

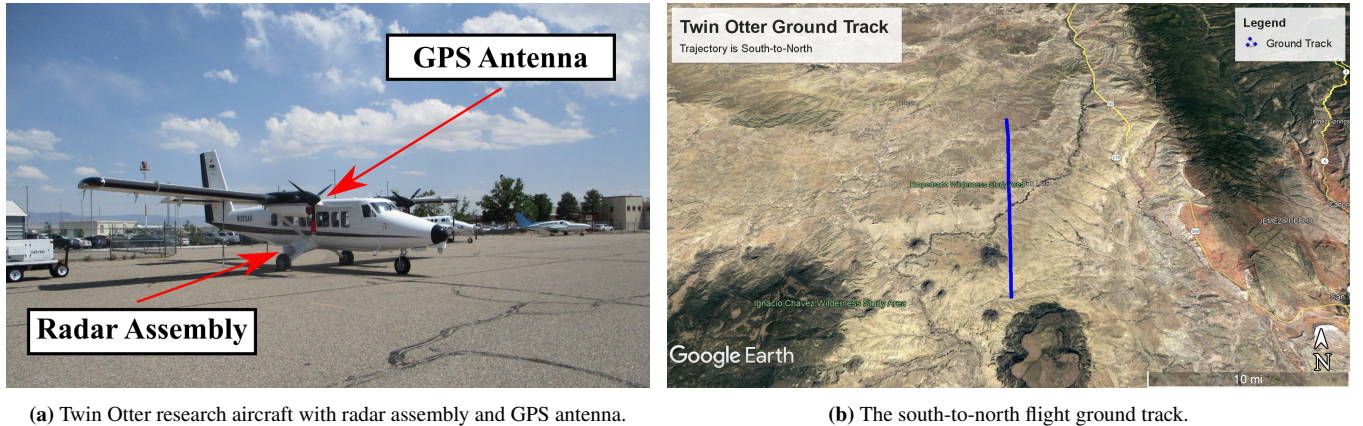
$$\mathbf{H} = [\tilde{\mathbf{H}}, \mathbf{0}_{L \times 9}] \quad (79)$$

V. FLIGHT DEMONSTRATION

The following section presents post-processed results from a flight demonstration of the VSAR / TITAN system over a wilderness area in central New Mexico.

1. Flight Overview

A gimbaled VSAR affixed to a Twin Otter research aircraft captured a series of VSAR range-Doppler images while flying along a straight line at a constant altitude over a wilderness area northeast of Mount Taylor in central New Mexico. The radar pulses and gimbal were controlled by a high-fidelity motion measurement system driven at 100 Hz by a Honeywell HG9900 IMU and corrected by a Novatel GPS receiver receiving real-time TerraStar-C differential corrections. The HG9900 is mounted directly to the backplane of the radar and the two sensors are assumed to be coincident and frame-aligned. The ground-truth trajectory was determined by post-processing the IMU and GPS data, and the resulting 1σ position & velocity standard deviations are approximately 5 cm and 1 cm/s respectively.



(a) Twin Otter research aircraft with radar assembly and GPS antenna.

(b) The south-to-north flight ground track.

Figure 6: The Twin Otter research aircraft (left) and flight ground track (right).

Fig. 6 shows the Twin Otter research aircraft (left) and the aircraft's ground track (right) plotted in Google Earth. A total of 207 VSAR range-Doppler images were captured by the aircraft over a period of about five minutes. VSAR images were produced approximately every 1.5 seconds at altitude of 15 kft and approximate ground clearance of 9 kft. The overflowed wilderness area is characterized by minimal vegetation and structures. The terrain elevation varied by a total of 1000 ft over the 14 mile flight.

The radar phase history was captured at the time and post-processed into range-Doppler images. It is important to note that the high-fidelity motion measurement system controlled and corrected the radar pulses, ensuring that produced radar images were of high quality [Doerry, 2015]. That is, while the following results will demonstrate navigation without the aid of GPS, *the radar images were formed with the aid of GPS*. This choice was intentional — there were sufficient problems to overcome related to the TITAN algorithm without introducing large, correlated errors the measurement and error state vectors. Future work will remove GPS entirely and will focus on characterizing the closed-loop, sans-GPS stability of a INS-VSAR navigator.

2. Map Pre-Processing

A 1/3 arc-second digital terrain elevation model provided by the United States Geological Survey (USGS) was used to predict / correlate the VSAR range-Doppler measurements [U.S. Geological Survey, 2022]. The published DEM is a square 1-degree longitude by 1-degree latitude tile, and the elevation posts are offset by a constant angular unit (1/3 arc-second). The map elevation posts are referenced to the North America Datum 1988 (NAVD88) — a local geoidal datum rather than an ellipsoidal datum. While none of these qualities preclude VSAR measurement prediction, they certainly complicate it, and it is preferred

that the reference terrain elevation data has constant post spacing in unit meters and is referenced to the WGS84 ellipsoid.

The USGS DEM tile was projected, interpolated, and corrected so that it adhered to the meter and WGS84-referenced preferences. First, NAVD88, GEOID 18, Grid 6 geoidal corrections provided by the National Oceanic and Atmospheric Administration (NOAA) were added to the USGS post elevations so that the post vertical datum was referenced against the WGS84 ellipsoid [U.S. National Oceanic and Atmospheric Administration, 2023]. Next, the DEM tile was projected onto a Universal Transverse Mercator (UTM) plane using the UTM projection equations defined in ‘Map Projections: A Working Manual’ [Snyder, 1987]. During this projection, the DEM posts were linearly resampled to be 10 meters in Easting and Northing — approximately the same spatial resolution of the original 1/3 arc-second posts. Finally, the UTM DEM was linearly resampled to 2-meter resolution to mitigate the quantization effects of the reference map data. Fig. 7 plots the resulting 2-meter map and overlays the flight ground track.

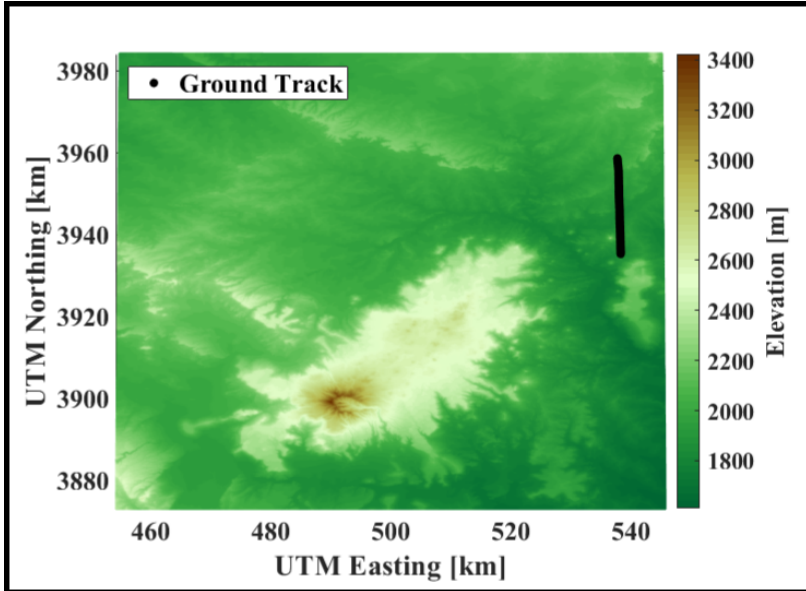


Figure 7: UTM-projected USGS DEM tile.

3. TITAN Design & Tuning

The following subsection lists the navigation parameters and rationalizes the EKF tuning choices. The TITAN navigator was driven by the same HG9900 used to form the radar images (this technically introduces a correlation between the sensor measurement and the error states, though it is believed to be negligibly small because the differential GPS aiding). The HG9900 gyroscope parameters were taken from Honeywell’s public brochure [Honeywell, 2023]. The HG9900 accelerometer bias was taken from the brochure and multiplied by a factor of 10 to account for a poor calibration of the sensor. The HG9900 accelerometer power spectral density (PSD) is missing from the brochure, and so a navigation-grade textbook value was substituted [Brown and Hwang, 1997]. The modeled IMU parameters are tabulated in Table 1:

Table 1: Modeled Honeywell HG9900 Parameters

1σ Accelerometer Bias	$10 \cdot 25 \mu\text{g}$
Accelerometer Root-PSD	$0.01 \text{ mg}/\sqrt{\text{Hz}}$
1σ Gyroscope Bias	$0.0035 \text{ deg}/\text{hr}$
Gyroscope Root-PSD	$0.002 \text{ deg}/\sqrt{\text{hr}}$

The SNL testbed radar operated at Ku-band and produced 207 VSAR images with a range resolution of approximately 3 meters and a Doppler resolution of approximately 14 Hz (approximately 5 meters in the along-track direction when projected onto the ground). The radar was modeled with a 12-degree circular sharp beam width (it can only detect points within ± 6 degrees). A total of 11 Doppler bins were prescribed with Doppler extents equal to the 14 Hz Doppler resolution. The Doppler bins were prescribed such that their center frequencies corresponded with along-track angles uniformly spaced at 0.5-degree increments between -2.5 degrees and +2.5 degrees. The along-track angle ϕ is related to the Doppler frequency Δf and aircraft velocity v

as

$$\Delta f = 2 \frac{f_c}{c} \|\mathbf{v}\| \sin(\phi)$$

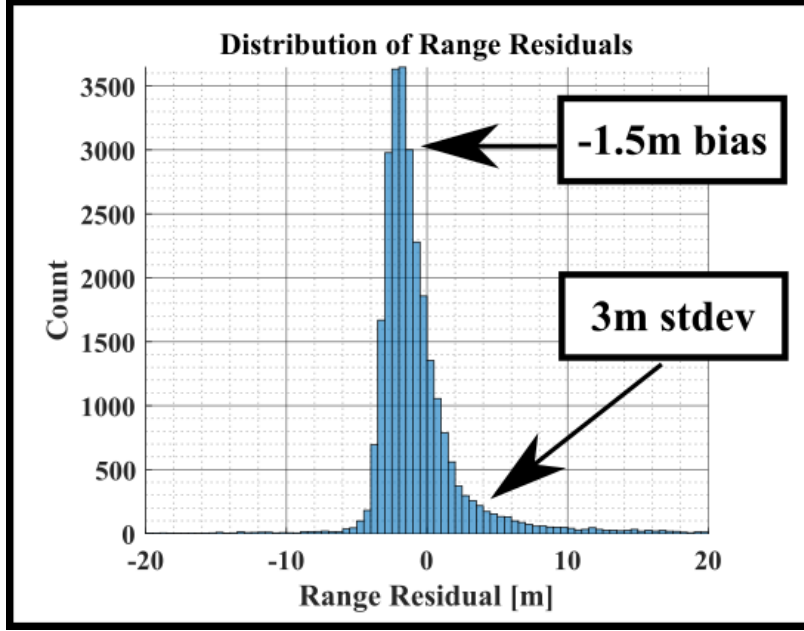


Figure 8: Distribution of the range residuals when measurements were predicted using the ground-truth position, velocity, and attitude.

To conform to EKF assumptions, the TITAN measurements should be modeled as corrupted by zero-mean Gaussian noise. No model has yet been developed for the range measurement noise which must capture the combined effects range noise, range bias, and errors in the map, among other factors. Future work will focus on developing such a model. For now, the modeled range noise is determined empirically from range residuals determined as the difference between the captured measurements and the measurements predicted at the ground-truth-logged position, velocity, and attitude. Fig. 8 plots these residuals and their statistics quantified by a robust covariance analysis [Rousseeuw and Driessen, 1999]. The residuals are biased by approximately -1.5 meters — that is, the measured ranges were on average 1.5 meters *smaller* than the predicted ranges. The cause of this bias is currently unknown — perhaps a map bias or the average effect of unmapped foliage. Because a bias is currently unmodeled in the measurement function, the VSAR range measurements were bulk corrected by +1.5 meters to prevent mis-attribution of the residuals to other navigation states. Future work will attempt to locate the source of the bias and either remove it or include it as a state in the measurement model. The robust covariance analysis determined the robust standard residual standard deviation to be approximately 3 meters, but it is clear that the residual distribution has heavy and asymmetrical tails.

Given the residual analysis above, the 11 TITAN MRPD measurements were modeled as corrupted by independent zero-mean Gaussian noise with a standard deviation of 6 meters — twice the standard deviation calculated by the robust covariance analysis. The standard deviation was inflated to de-weight the range measurements as a cautionary step to mitigate the effects of non-linearities and unmodeled errors [Carpenter and D’Souza, 2018].

A snapshot innovations monitor rejected any individual scalar measurement whose normalized innovation ($\hat{y}_i := y_i / \sqrt{S_{(i,i)}}$) exceeded a magnitude of 1.5. Typically, normalized innovations are rejected at a magnitude of 3 or greater, but since the modeled measurement error covariance was inflated by a factor of 2, it was deemed appropriate to reduce the threshold by the same factor.

The IMU bias states were modeled as Schmidt states and ‘considered’ [Zanetti and D’Souza, 2013]. That is, during the Kalman update and prior to the calculation of the Kalman correction, the Kalman gain values associated with the accelerometer and gyroscope biases were zeroed out. The resulting computed Kalman correction for the IMU bias states was zero. The intention here is to prevent non-linearities or model errors in the VSAR measurements from being incorrectly attributed to the IMU bias states. Because the bias states are modeled as constant and have no process noise, any correction to them — whether correct or incorrect — is nearly permanent. Thus, as a safety mechanism to prevent a permanent model error, the IMU states were ‘considered’. Here, the term ‘considered’ means that these bias states still inflate the process noise of the position, velocity, and attitude states like in a standard INS, but they are never corrected during a Kalman update.

Finally, the navigator was initialized at the ground-truth position, velocity, and attitude one-minute before the start of terrain-aided navigation. The nominal initial bias states were set to zero. The modeled error covariance was initialized

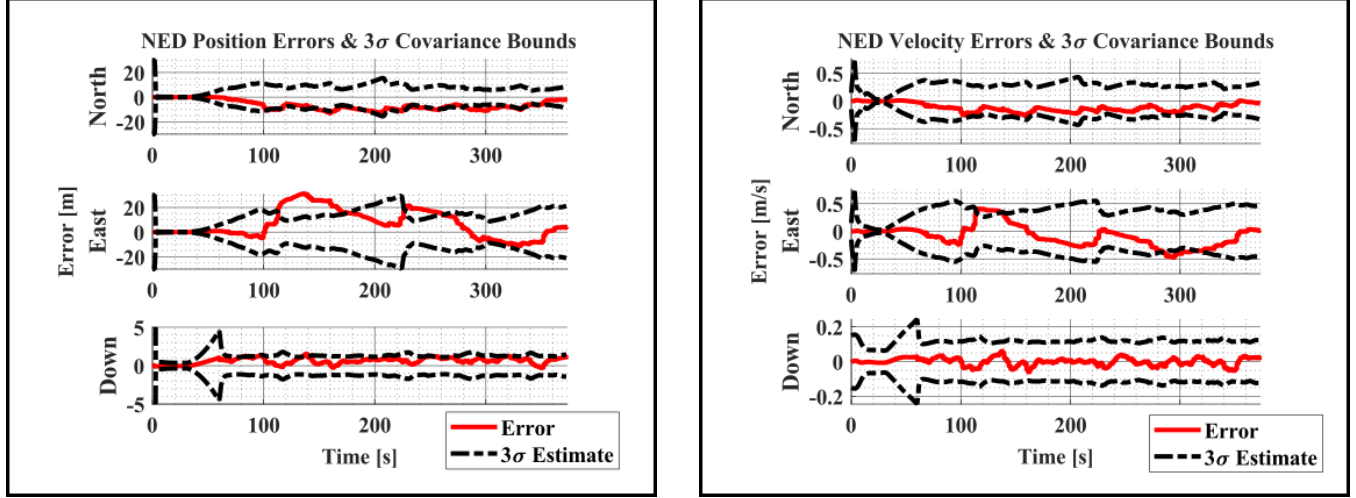
$$\mathbf{P} = \begin{bmatrix} \mathbf{P}_p & \mathbf{0}_{3 \times 3} & \mathbf{0}_{3 \times 3} & \mathbf{0}_{3 \times 3} & \mathbf{0}_{3 \times 3} \\ \mathbf{0}_{3 \times 3} & \mathbf{P}_v & \mathbf{0}_{3 \times 3} & \mathbf{0}_{3 \times 3} & \mathbf{0}_{3 \times 3} \\ \mathbf{0}_{3 \times 3} & \mathbf{0}_{3 \times 3} & \mathbf{P}_a & \mathbf{0}_{3 \times 3} & \mathbf{0}_{3 \times 3} \\ \mathbf{0}_{3 \times 3} & \mathbf{0}_{3 \times 3} & \mathbf{0}_{3 \times 3} & \mathbf{P}_{ab} & \mathbf{0}_{3 \times 3} \\ \mathbf{0}_{3 \times 3} & \mathbf{0}_{3 \times 3} & \mathbf{0}_{3 \times 3} & \mathbf{0}_{3 \times 3} & \mathbf{P}_{gb} \end{bmatrix} \quad (80)$$

where $\mathbf{P}_p = (10 \text{ m})^2 \cdot \mathbf{I}_{3 \times 3}$, $\mathbf{P}_v = (50 \text{ cm/s})^2 \cdot \mathbf{I}_{3 \times 3}$, $\mathbf{P}_a = (0.5 \text{ deg})^2 \cdot \mathbf{I}_{3 \times 3}$, $\mathbf{P}_{ab} = (10 \cdot 25 \mu\text{g})^2 \cdot \mathbf{I}_{3 \times 3}$, and $\mathbf{P}_{gb} = (0.0035 \text{ deg/hr})^2 \cdot \mathbf{I}_{3 \times 3}$.

For the first 30 seconds of the flight, the navigator was aided by the TerraStar-C GPS measurements. Then, for the next 30 seconds, GPS was disabled and the navigator coasted on the IMU measurements. The goal of this large initial covariance coupled with a brief period of GPS measurements was to put the navigator in a ‘steady state’ with realistic covariance values between the error states; the goal of the free-inertial period was to allow the navigator to accumulate sufficient error that it wouldn’t immediately de-weight the initial VSAR measurements as it came off a differential GPS navigation solution.

4. Navigation Results

Fig. 9 plots the position and velocity navigation errors in the North-East-Down (NED) frame. Note that the trajectory traveled from south-to-north and so north, east, and down also correspond with along-track, cross-track, and down, respectively. The navigation errors are given by the red line and the corresponding 3σ covariance bounds by the dashed black lines.



(a) The NED position errors (red) and 3σ error covariance bounds (black dashed).

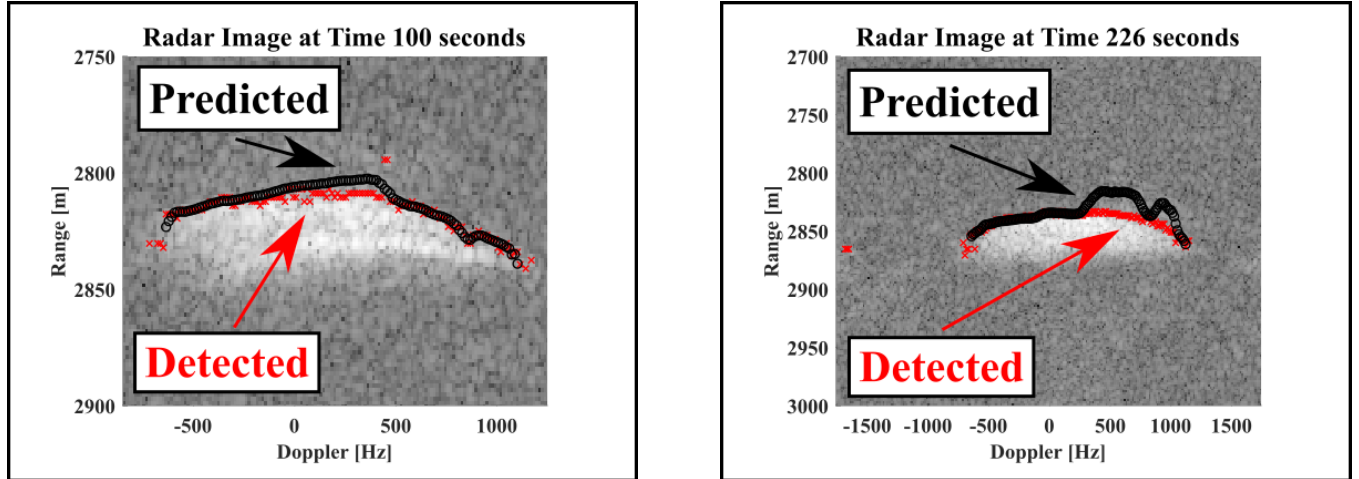
(b) The NED velocity errors (red) and 3σ error covariance bounds (black dashed).

Figure 9: The NED position errors (left) and velocity errors (right).

The navigation results show that the errors are bounded, and for the most part reasonably characterized by the 3σ error covariance bounds. The north/along-track position and velocity estimates exhibited a bias of approximately 6 meters and 20 cm/s, respectively. The east/cross-track position and velocity estimates were not consistently biased, though they wandered significantly away from zero. The root-mean-square NED position error was [7.5, 13.1, 0.7] meters; the root-mean-square NED velocity error was [13.8, 21.6, 2.2] cm/s.

For two periods of time, the east/cross-track position deviated from its 3σ estimated error covariance bounds. These walks corresponded with large initial jumps in the position error around times 100 and 226 seconds. Scrutinizing these measurements and residuals, it is clear that these jumps were caused by either a missed detection or map error. Fig. 10 plots the two radar images at these times and overlays the detected minimum range contour and the contour predicted with the 2-meter map and ground-truth logged position, velocity, and attitude. It is clear that at these two time points, the MRPD predictions and detections diverged significantly. The root cause of these divergences likely lies either with the map — it may be inaccurate — or with

the radar sensor — it was unable to detect some important terrain features at these times. Future work will develop tools to automatically identify and mitigate error events such as these.



(a) Map-predicted and radar-detected MRPD measurements at time $t=100$ s.

(b) Map-predicted and radar-detected MRPD measurements at time $t=226$ s.

Figure 10: Map-predicted and radar-detected MRPD measurements at the two instances of large cross-track error growth.

Despite these two error events, the TITAN algorithm was able to maintain reasonable navigation performance and even recover a navigation solution bounded by the 3σ error covariance bounds. Future work will improve outlier detection and mitigation strategies which will enable tighter tuning of the modeled error covariance bounds and improved navigation performance.

VI. CONCLUSIONS & FUTURE WORK

The Vertical Synthetic Aperture Radar was introduced as a potential navigation sensor, and the Trusted Inertial Terrain-Aided Navigation algorithm was suggested as a companion navigation algorithm. The VSAR/TITAN combination was demonstrated with post-processed radar flight data and it was shown that the resulting sans-GPS navigation solution was accurate to within approximately 15 meters. Several areas of future work were identified: (1) analytical MRPD gradients; (2) an adaptive threshold MRPD detection algorithm; (3) tightly-coupled, sans-GPS INS-VSAR navigation; (4) and improved measurement outlier detection and mitigation algorithms. Each of these are expected to improve the performance and reliability of the VSAR/TITAN system.

ACKNOWLEDGMENTS

Tucker would like to thank the two technical mentors who have guided him in the ways of inertial navigation and radar signal processing: Ted Kim & Bill Hensley. Tucker would also like to thank Brandon Conder for his processing of the radar images and for his instruction on the fundamentals of radar signal processing.

This article has been authored by an employee of National Technology & Engineering Solutions of Sandia, LLC under Contract No. DE-NA0003525 with the U.S. Department of Energy (DOE). The employee owns all right, title and interest in and to the article and is solely responsible for its contents. The United States Government retains and the publisher, by accepting the article for publication, acknowledges that the United States Government retains a non-exclusive, paid-up, irrevocable, worldwide license to publish or reproduce the published form of this article or allow others to do so, for United States Government purposes. The DOE will provide public access to these results of federally sponsored research in accordance with the DOE Public Access Plan <https://www.energy.gov/downloads/doe-public-access-plan>.

This paper describes objective technical results and analysis. Any subjective views or opinions that might be expressed in the paper do not necessarily represent the views of the U.S. Department of Energy or the United States Government. SAND2023-0908C

REFERENCES

- [fed, 1974] (1974). Federal Register. <https://tile.loc.gov/storage-services/service/11/fedreg/fr039/fr039248/fr039248.pdf>. Date Accessed: 20230824.
- [Arasaratnam and Haykin, 2009] Arasaratnam, I. and Haykin, S. (2009). Cubature Kalman filters. *IEEE Transactions on automatic control*, 54(6):1254–1269.
- [Brown and Hwang, 1997] Brown, R. G. and Hwang, P. Y. (1997). Introduction to random signals and applied Kalman filtering: with MATLAB exercises and solutions. *Introduction to random signals and applied Kalman filtering: with MATLAB exercises and solutions*.
- [Carpenter and D’Souza, 2018] Carpenter, J. R. and D’Souza, C. N. (2018). Navigation filter best practices. Technical report.
- [Carroll and Canciani, 2021] Carroll, J. D. and Canciani, A. J. (2021). Terrain-referenced navigation using a steerable-laser measurement sensor. *Navigation*, 68(1):115–134.
- [Choi et al., 2013] Choi, S., Chun, J., Paek, I., and Yoo, K. (2013). A new approach of FMCW-DBS altimeters for terrain-aided navigation. In *Conference Proceedings of 2013 Asia-Pacific Conference on Synthetic Aperture Radar (APSAR)*, pages 214–217. IEEE.
- [Cumming and Wong, 2005] Cumming, I. G. and Wong, F. H. (2005). *Digital processing of synthetic aperture radar data*, volume 1. Boston.
- [Doerry, 1994] Doerry, A. W. (1994). Patch diameter limitation due to high chirp rates in focused SAR images. *IEEE Transactions on Aerospace and Electronic Systems*, 30(4):1125–1129.
- [Doerry, 1995] Doerry, A. W. (1995). Synthetic aperture radar processing with tiered subapertures.
- [Doerry, 2015] Doerry, A. W. (2015). Motion measurement for synthetic aperture radar. Technical report, Sandia National Lab.(SNL-NM), Albuquerque, NM (United States).
- [Gaudet and Furfaro, 2013] Gaudet, B. and Furfaro, R. (2013). A navigation scheme for pinpoint mars landing using radar altimetry, a digital terrain model, and a particle filter. In *Proc. AAS/AIAA Astrodynamics Specialist Conf.*, pages 2537–2556.
- [Golden, 1980] Golden, J. P. (1980). Terrain contour matching (TERCOM): a cruise missile guidance aid. In *Image processing for missile guidance*, volume 238, pages 10–18. SPIE.
- [Groves, 2013] Groves, P. D. (2013). *Principles of GNSS, Inertial, and Multisensor Integrated Navigation Systems, Second Edition*. Artech House, Boston, London.
- [Hollowell, 1990] Hollowell, J. (1990). Heli/SITAN: A terrain referenced navigation algorithm for helicopters. Technical report, Sandia National Lab.(SNL-NM), Albuquerque, NM (United States).
- [Honeywell, 2023] Honeywell (2023). HG9900 Inertial Measurement Unit. <https://aerospace.honeywell.com/content/dam/aerobt/en/documents/learn/products/sensors/brochures/N61-1638-000-000-hg9900inertialmeasurementunit-bro.pdf>. Date Accessed: 20230824.
- [Hostetler and Andreas, 1983] Hostetler, L. and Andreas, R. (1983). Nonlinear Kalman filtering techniques for terrain-aided navigation. *IEEE Transactions on Automatic Control*, 28(3):315–323.
- [Johnson and Ivanov, 2011] Johnson, A. and Ivanov, T. (2011). Analysis and testing of a lidar-based approach to terrain relative navigation for precise lunar landing. In *Aiaa guidance, navigation, and control conference*, page 6578.
- [Johnson et al., 2022] Johnson, A. E., Aaron, S. B., Ansari, H., Bergh, C., Bourdu, H., Butler, J., Chang, J., Cheng, R., Cheng, Y., Clark, K., et al. (2022). Mars 2020 lander vision system flight performance. In *AIAA SciTech 2022 Forum*, page 1214.
- [Kim et al., 2018] Kim, Y., Park, J., and Bang, H. (2018). Terrain-Referenced Navigation using an Interferometric Radar Altimeter. *NAVIGATION: Journal of the Institute of Navigation*, 65(2):157–167.
- [Lee et al., 2020] Lee, J., Sung, C.-K., Oh, J., Han, K., Lee, S., and Yu, M.-J. (2020). A pragmatic approach to the design of advanced precision terrain-aided navigation for UAVs and its verification. *Remote Sensing*, 12(9):1396.
- [Lindstrom et al., 2022] Lindstrom, C., Christensen, R., Gunther, J., and Jenkins, S. (2022). GPS-denied navigation aided by synthetic aperture radar using the range-Doppler algorithm. *NAVIGATION: Journal of the Institute of Navigation*, 69(3).
- [Oh et al., 2019] Oh, J., Sung, C.-K., Lee, J., Lee, S. W., Lee, S. J., and Yu, M.-J. (2019). Accurate measurement calculation method for interferometric radar altimeter-based terrain referenced navigation. *Sensors*, 19(7):1688.

- [Pogorelsky et al., 2022] Pogorelsky, B. S., Zanetti, R., Chen, J., and Jenkins, S. (2022). Synthetic-Aperture-Radar-Based Spacecraft Terrain Relative Navigation. *Journal of Spacecraft and Rockets*, 59(5):1412–1424.
- [Reed et al., 1980] Reed, C., Kohn, J., and Mercier, D. (1980). The Range Only Correlation System. In *Image Processing for Missile Guidance*, volume 238, pages 42–49. SPIE.
- [Rousseeuw and Driessen, 1999] Rousseeuw, P. J. and Driessen, K. V. (1999). A fast algorithm for the minimum covariance determinant estimator. *Technometrics*, 41(3):212–223.
- [Snyder, 1987] Snyder, J. P. (1987). *Map projections—A working manual*, volume 1395. US Government Printing Office.
- [U.S. Geological Survey, 2022] U.S. Geological Survey (2022). Usgs 1/3 arc second n36w108 20220801. <https://www.sciencebase.gov/catalog/item/63045f6ad34ed6dc5592a7e1>.
- [U.S. National Oceanic and Atmospheric Administration, 2023] U.S. National Oceanic and Atmospheric Administration (2023). Geoid18 grids for conterminous united states (conus). <https://geodesy.noaa.gov/GEOID/GEOID18/downloads.shtml>. Date Accessed: 20230824.
- [Yoder and Humphreys, 2023] Yoder, J. E. and Humphreys, T. E. (2023). Low-Cost Inertial Aiding for Deep-Urban Tightly Coupled Multi-Antenna Precise GNSS. *NAVIGATION: Journal of the Institute of Navigation*, 70(1).
- [Zanetti and D’Souza, 2013] Zanetti, R. and D’Souza, C. (2013). Recursive implementations of the Schmidt-Kalman ‘consider’ filter. *The Journal of the Astronautical Sciences*, 60(3-4):672–685.
- [Zhao et al., 2014] Zhao, L., Gao, N., Huang, B., Wang, Q., and Zhou, J. (2014). A novel terrain-aided navigation algorithm combined with the TERCOM algorithm and particle filter. *IEEE Sensors Journal*, 15(2):1124–1131.